Growth of Large-Area 2D $MoS_{2(1-x)}Se_{2x}$ Semiconductor Alloys

Qingliang Feng, Yiming Zhu, Jinhua Hong, Mei Zhang, Wenjie Duan, Nannan Mao, Juanxia Wu, Hua Xu, Fengliang Dong, Fang Lin, Chuanhong Jin, Chunming Wang, Jin Zhang, and Liming Xie**

Two-dimensional (2D) semiconductors—a new family of materials with atomic thickness but without dangling bonds on their surface—have attracted intense interest because of their potential applications in nano- and opto-electronics.[1–10] 2D semiconductor alloys can have tunable bandgaps in wide spectrum ranges; this has been both proposed by theoretical calculations[11,12] and demonstrated by experiments in transition-metal dichalcogenide monolayer alloys.[13] Similar to applications of graphene,[14–17] practical applications of 2D semiconductor alloys require the synthesis of large-area samples. Several approaches, such as chemical vapor deposition (CVD)[18–22] and physical vapor deposition (PVD),[23] have been used to grow 2D semiconductors with a controlled number of layers and large crystal domains; however, the large-area growth of 2D semiconductor alloys has not yet been reported—probably because of the challenges in controlling atom-mixing within the monolayer and in chemically imaging the elemental distribution at atomic scale. Here we report the synthesis of large-area 2D semiconductor alloys comprising $MoS_{2(1-x)}Se_{2x}$ monolayers, where x = 0–0.40. Atomic-resolution high-angle annular dark-field (HAADF) scanning transmission electron microscopy (STEM) imaging revealed a random arrangement of the S and Se atoms in the 2D alloys. The bandgap photoluminescence (PL) is continuously tuned from 1.86 eV (i.e., 665 nm, reached with x = 0) to 1.73 eV (i.e., 716 nm, reached with x = 0.40). Field-effect transistors (FETs) fabricated on the $MoS_{2(1-x)}Se_{2x}$ monolayer alloys exhibit high on/off ratios of $>10^5$. These 2D semiconductor alloy films have potential applications in flexible light-detection and light-harvesting devices.

Q. Feng,[+] W. Duan, N. Mao, J. Wu, Dr. H. Xu, Prof. J. Zhang
Center for Nanochemistry
Beijing National Laboratory for Molecular Sciences
Key Laboratory for the Physics and Chemistry of Nanodevices
State Key Laboratory for Structural Chemistry of Unstable and Stable Species
College of Chemistry and Molecular Engineering
Peking University
Beijing 100871, P. R. China
E-mail: jinzhang@pku.edu.cn

Q. Feng, Y. Zhu,[+] M. Zhang, N. Mao, Dr. F. Dong, Prof. L. Xie
CAS Key Laboratory of Standardization and Measurement for Nanotechnology
National Center for Nanoscience and Technology
Beijing 100190, P. R. China
E-mail: xielm@nanoctr.cn

J. Hong, Prof. C. Jin
State Key Laboratory of Silicon Materials
Key Laboratory of Advanced Materials and Applications for Batteries of Zhejiang Province and Department of Materials Science and Engineering
Zhejiang University
Hangzhou 310027, P. R. China

Q. Feng, Prof. C. Wang
School of Chemistry and Chemical Engineering
Lanzhou University
Lanzhou 730000, P. R. China

Prof. F. Lin
College of Science
South China Agricultural University
Guangzhou 510642, P. R. China

[+]These authors contributed equally to this work.

DOI: 10.1002/adma.201306095

Figure 1 illustrates the low-pressure, three-zone furnace used in the growth of the $MoS_{2(1-x)}Se_{2x}$ monolayer. $MoSe_2$ and MoS_2 powders were put in the first and second zones, respectively, at temperatures of $T = T1$ and $T2$, respectively, and directly vaporized at high temperatures (T = 940–975 °C). SiO_2/Si substrates with an oxide thickness of ~270 nm were put in the third zone (T = ~600–700 °C) with a temperature gradient of ~50 °C/cm to allow growth of the $MoS_{2(1-x)}Se_{2x}$ monolayers. By finely tuning the growth conditions, such as evaporation temperature (see Supporting Information (SI): Figure S1), gradient of deposition temperature (SI: Figure S2), and H_2 flow rate in the carrier gases (SI: Figure S3), high-quality $MoS_{2(1-x)}Se_{2x}$ monolayers were grown on SiO_2/Si substrates.

Figure 2a shows an optical image of as-grown MoS_2 and $MoS_{1.60}Se_{0.40}$ films. The Se composition in the $MoS_{2(1-x)}Se_{2x}$ monolayers was determined by X-ray photo-emission spectroscopy (XPS; Figure 2g). The colors of the MoS_2 and $MoS_{1.60}Se_{0.40}$ monolayer films are different from that of the bare substrate (SiO_2/Si). By controlling the loading of the evaporation sources (MoS_2 and $MoSe_2$ powders), the coverage of the $MoS_{1.60}Se_{0.40}$ monolayers can be tuned (Figure 2b,c). With small amounts loaded, triangles of $MoS_{1.60}Se_{0.40}$ monolayers with sizes of >2 μm were obtained. With large amounts, continuous films of $MoS_{1.60}Se_{0.40}$ monolayers were obtained. Atomic force microscopy (AFM) characterization showed a height of around 1.0 nm for the as-grown $MoS_{1.60}Se_{0.40}$ films (Figure 2d), indicating the monolayer thickness of the films. The bandgap emission energy of the $MoS_{1.60}Se_{0.40}$ monolayer is ~1.79 eV (i.e., 692 nm; Figure 2e), which is smaller than that of the MoS_2 monolayer[24] (~1.86 eV, i.e., 665 nm), as expected.[11] PL and Raman mapping also indicate homogeneous compositions over large areas (SI: Figure S4).

Four Raman peaks were observed from the $MoS_{1.60}Se_{0.40}$ monolayers (Figure 2f). Two peaks at 403 and 380 cm^{-1} are assigned to the A_1' and E' modes related to MoS_2,[25] respectively. Polarized Raman spectra confirmed the assignment, in which the A_1' was only observed in the $Z(XX)\bar{Z}$ configuration, and not at the $Z(XY)Z$ configuration, while the E' was observed at both the $Z(XX)\bar{Z}$ and $Z(XY)\bar{Z}$ configurations,

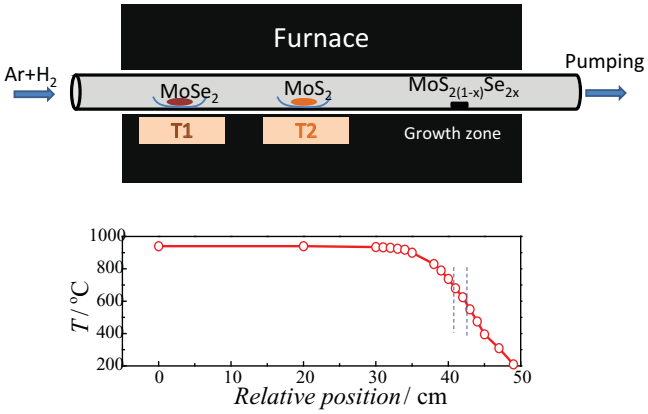

Figure 1. Illustration of three-zone furnace for the growth of the $MoS_{2(1-x)}Se_{2x}$ monolayer (upper panel), and the temperature profile along the growth tube (bottom panel). The blue dashed lines indicate the growth zone region.

matching the selection rules derived from the corresponding polarization tensors.[26,27] The Raman peaks at 271 and 363 cm^{-1} were only present in the $Z(XX)\bar{Z}$ configuration. Confirmative assignment of the two peaks would require the peak frequency changes throughout the entire Se composition (i.e., $x = 0$–1, but currently only $x = 0$ to 0.40 is achieved). The peak at 271 cm^{-1} could be the $MoSe_2$-like A_1' mode, considering that the A_1' mode of the $MoSe_2$ monolayer is at 242 cm^{-1}.[28]

To image the distribution of the S and Se atoms in the $MoS_{1.60}Se_{0.40}$ monolayers, HAADF-STEM imaging was conducted (**Figure 3**); HAADF-STEM can provide Z-contrast images with atomic lateral resolution (Z = atomic number).[29,30] In Figure 3a, the Mo sites and bi-chalcogen (X_2) sites can be easily discriminated (see also the SI: Figure S5). All Mo sites have similar brightness and are brighter than most of the X_2 sites because the Z number of Mo (42) is larger than those of S (16) and Se (34). The intensity histograms of the Mo and X_2 sites are shown in Figure 3b, Three intensity regions can be found for the X_2 sites: the dimmest regions with an intensity of ~40–125 arbitrary units (a.u.), the medium-brightness region with an intensity of 125–210 a.u., and the brightest region with an intensity of >210 a.u. The three regions are assigned to S_2, SSe, and Se_2 sites, respectively. By counting individual sites (SI: Figure S5), the Se atom percentage can be obtained (152/796 = 0.19), matching well with the XPS result of $x = 0.20$ for the Se composition.

Furthermore, color rendering is used for better visualizing the different X_2 sites (Figure 3c,d; S_2 sites: light blue; SSe sites: yellow; Se_2 sites: red). A structural schematic can be drawn (Figure 3d), and different coordination configurations of the Mo atoms can be clearly seen (as triangles in Figure 3d). The Mo atom can have $3S_2$ coordination, $2S_2$ + 1SSe coordination, $2S_2$ + $1Se_2$ coordination, $1S_2$ + 2SSe coordination, and so on. Figure 3e plots the probabilities of finding the different coordination configurations. Assuming a random arrangement of S and Se atoms around Mo, the probability of finding a certain configuration can be calculated by the binomial distribution[31]

$$P(n,N,x) = \frac{N!}{n!(N-n)!}x^n(1-x)^{N-n} \quad (1)$$

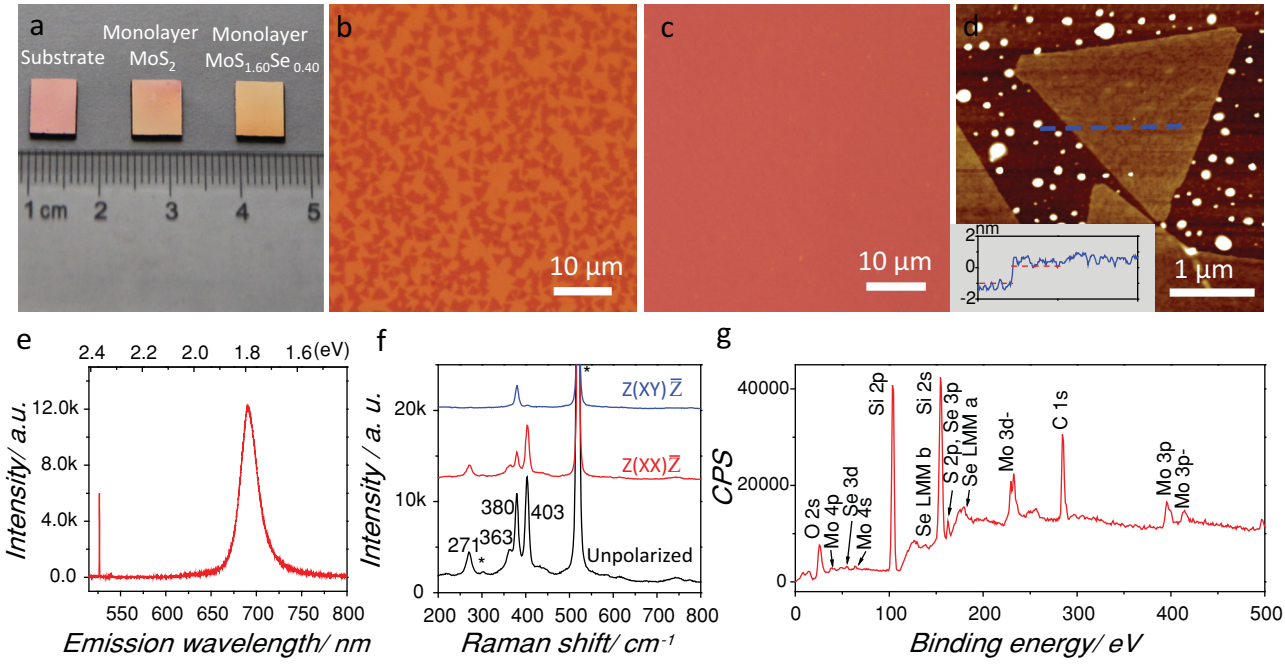

Figure 2. a) Photograph of bare SiO_2/Si substrate and MoS_2 and $MoS_{1.60}Se_{0.40}$ monolayer films on SiO_2/Si substrates. b,c) Optical images of as-grown $MoS_{1.60}Se_{0.40}$ monolayers: triangles (b) and continuous film (c). d) AFM image of $MoS_{1.60}Se_{0.40}$ triangles exhibit a height of ~1.0 nm. Inset shows the height profile along the dashed blue line. e) PL spectrum, f) polarized and unpolarized Raman spectra, and g) XPS spectrum of $MoS_{1.60}Se_{0.40}$ monolayers. In panel f, the Raman peaks labelled with * are from the SiO_2/Si substrate. The "k" in the axis scales of e and f refers to units of 1000. CPS in g is counts per second.

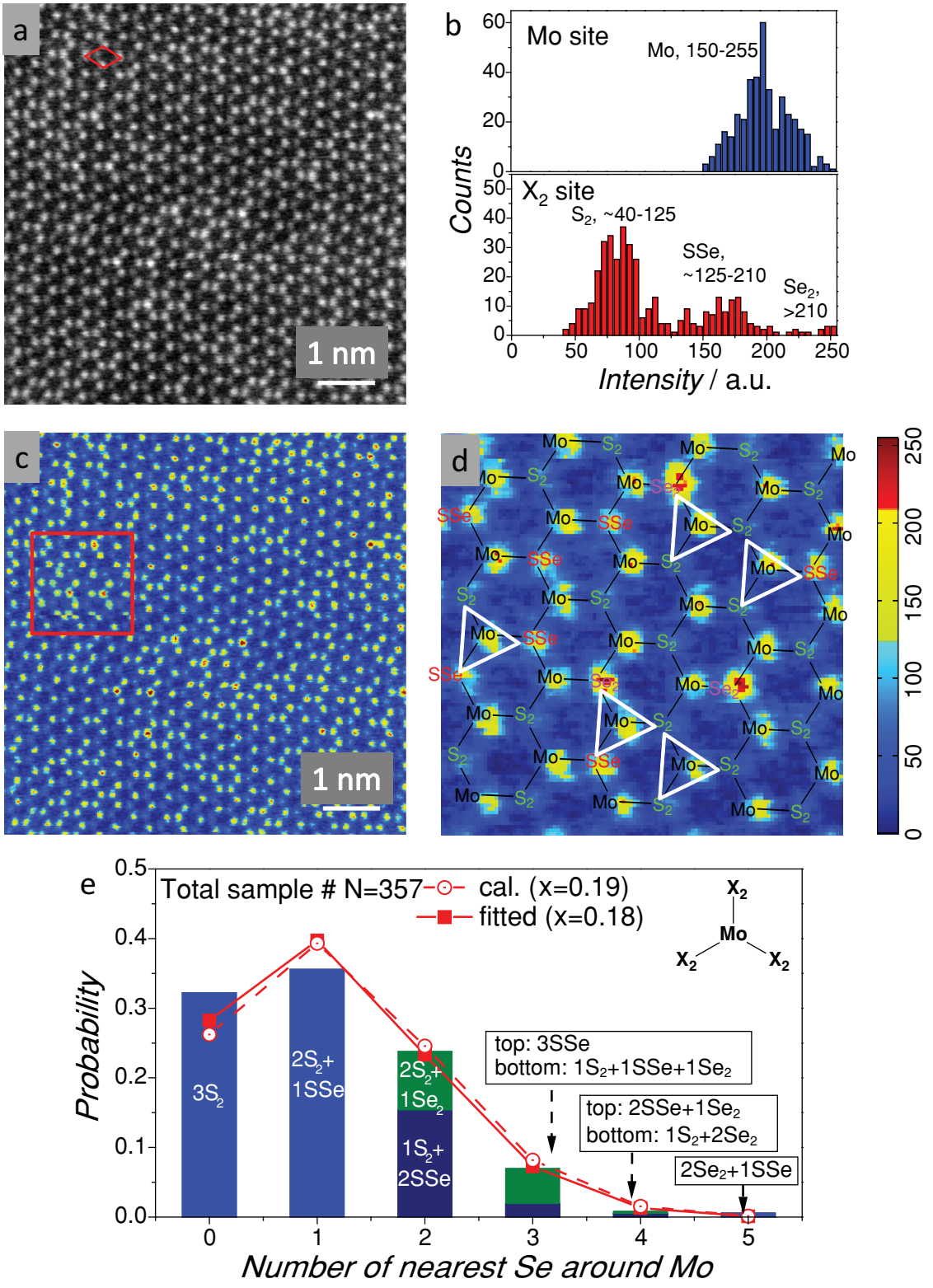

Figure 3. a) HAADF-STEM image of $MoS_{1.60}Se_{0.40}$ monolayer. The red rhombus show a unit cell with Mo atoms at the corners. b) Intensity histograms of atom sites in panel a. c,d) HAADF-STEM image in false color. Mo sites: yellow; S_2 sites: light blue; SSe sites: yellow, and Se_2 sites: red. The red square in c outlines the part of the image shown in d. The color scale shown in d is HAADF-STEM intensity in arbitrary units, in which different intensity ranges are shown in different colors. e) Probability of finding different coordination configurations. The open circles are the calculated probability using the binomial distribution with an *x* value of 0.19. The solid squares are the fitted values using the binomial distribution.

Table 1. Summary of growth conditions and A-exciton emission energy for all synthesized $MoS_{2(1-x)}Se_{2x}$ monolayers.

T1 [°C] for $MoSe_2$	*T2* [°C] for MoS_2	S/Se atom ratio from XPS	*x* value in $MoS_{2(1-x)}Se_{2x}$	A-exciton emission energy [eV] (corresponding emission wavelength [nm])
- (MoS_2 only)	940	- (S only)	0	1.862 ± 0.004 (665–670)
940	940	7.2/1	0.12	1.821 ± 0.007 (678–683)
945	940	4.8/1	0.15	1.808 ± 0.003 (685–687)
950	940	4.0/1	0.20	1.791 ± 0.004 (690–694)
955	940	3.0/1	0.25	1.790 ± 0.001 (692–693)
960	940	2.62/1	0.27	1.773 ± 0.004 (698–701)
965	940	2.32/1	0.30	1.756 ± 0.004 (704–708)
970	940	2.03/1	0.33	1.747 ± 0.005 (708–712 nm)
975	940	1.50/1	0.40	1.732 ± 0.005 (714–718 nm)

where *n* is the number of Se atoms around Mo in the configuration, *N* is the total coordination number ($N = 6$), and *x* is the probability of a coordination site occupied by Se. For a random distribution of Se atoms, *x* is related to the Se composition. The calculated probability (using $x = 0.19$ obtained from HAADF-STEM) matches experimental data very well (circled dots in Figure 3e). Furthermore, fitting the experimental data (solid squares in Figure 3e) can give an *x* value of 0.18, close to Se composition from HAADF-STEM ($x = 0.19$) and XPS ($x = 0.20$), suggesting a random distribution of S and Se atoms around Mo atoms.

By tuning the evaporation temperatures of MoS_2 and $MoSe_2$, the composition of as-synthesized $MoS_{2(1-x)}Se_{2x}$ monolayers can be finely controlled. **Table 1** summarizes growth conditions and the corresponding compositions and emission energies of the as-grown $MoS_{2(1-x)}Se_{2x}$ monolayers. At each growth condition, the emission wavelength has a variation of less than 5 nm. It was found that for the $MoS_{2(1-x)}Se_{2x}$ monolayers at locations with lower deposition temperature (i.e., downstream from the growth zone), the emission wavelength was systematically longer (i.e., lower energy), indicating slightly more Se in the composition at the locations further from the evaporation source. In our experiments, the highest Se composition achieved in $MoS_{2(1-x)}Se_{2x}$ monolayers is $x = 0.40$. At an even higher evaporation temperature for $MoSe_2$ (>975 °C), the as-grown $MoS_{2(1-x)}Se_{2x}$ films showed very small crystal domains (<200 nm), and the film thickness was thicker than a monolayer.

Figure 4a plots X-ray photo-electron spectra of all the as-synthesized $MoS_{2(1-x)}Se_{2x}$ monolayers. Quantification analysis of the Se 3d and S 2p peaks gives the Se compositions presented in Table 1. The A-exciton emission energy, from 1.86 to 1.73 eV (i.e., 665–716 nm, Figure 4b), monotonically

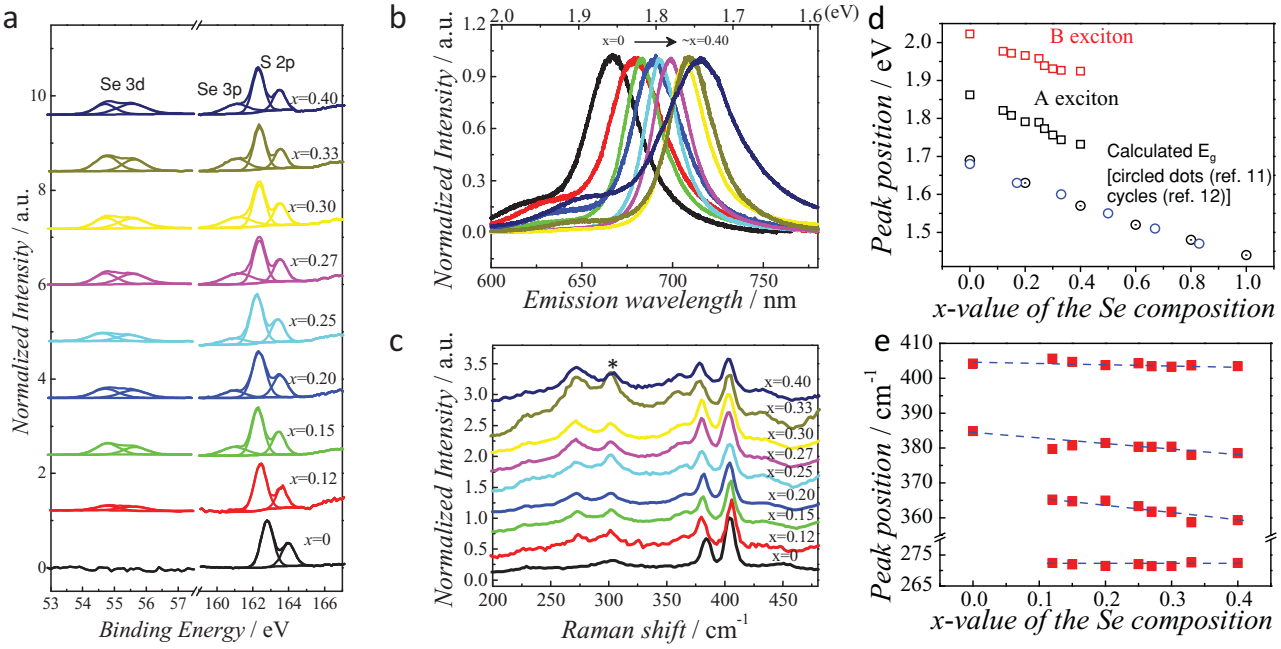

Figure 4. a) XPS, b) PL spectra, and c) Raman spectra of all as-grown $MoS_{2(1-x)}Se_{2x}$ monolayers. Again the * marks peaks due to the substrate. d,e) Plots of A- and B-exciton emission energy (d) and Raman frequency (e) against the *x*-value of the Se composition in $MoS_{2(1-x)}Se_{2x}$ monolayers.

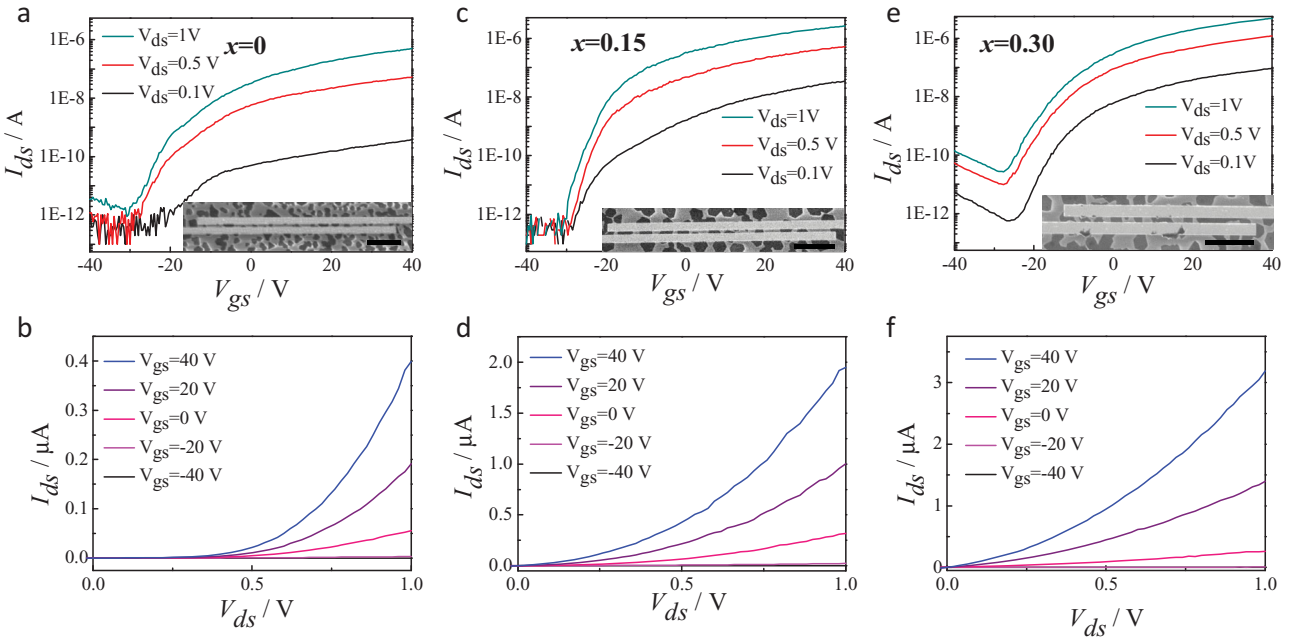

Figure 5. Plots of the a,c,e) source–drain current to the gate voltage (I_{ds} – V_{gs}) and b,d,f) the source–drain current to the source–drain voltage (I_{ds}–V_{ds}) for FETs containing the $MoS_{2(1-x)}Se_{2x}$ monolayer. a,b) for $x = 0$; c,d) for $x = 0.15$; e,f) for $x = 0.30$. The insets of (a),(c), and (e) show the SEM images of the device channel. Scale bars are 5 μm.

decreases as the Se composition increases, which is consistent with the calculated bandgap shift reported in the literature.[11,12] The bandgap bowing effect is not that obvious (Figure 4d) as it is in $Mo_{1-x}W_xS_2$ monolayers.[13] As the Se composition changes, the MoS_2-like A_1' mode (~403 cm^{-1}) and the peak at ~271 cm^{-1} show little shift (less than 1 cm^{-1}). While the MoS_2-like E' mode (~380 cm^{-1}) and the peak at ~360 cm^{-1} show a red-shift trend (Figure 4c,e).

FETs were also fabricated on $MoS_{2(1-x)}Se_{2x}$ monolayers (**Figure 5**). All $MoS_{2(1-x)}Se_{2x}$ monolayer devices exhibited n-type transport behavior[32] with high on/off ratios (>10^5; Figure 5a,c,e). The field-effect mobility μ_{FE} can be calculated by:[32]

$$\mu_{FE} = \frac{dI_{ds}}{dV_{gs}} \cdot \frac{L}{V_{ds} W C_g} \quad (2)$$

where I_{ds} is the source–drain current; V_{gs} is the gate–source voltage; V_{ds} is the source–drain voltage; L is the channel length; W is the channel width; and C_g is the gate capacitance. An average mobility of ~0.1 and ~0.4 $cm^2V^{-1}s^{-1}$ was estimated for the $MoS_{2(1-x)}Se_{2x}$-monolayer FETs with $x = 0.15$ and $x = 0.30$, respectively. A much lower mobility (<0.1 $cm^2V^{-1}s^{-1}$) was obtained for the MoS_2-monolayer FETs, which is due to its much poorer contact (Figure 5b) in comparison to that of the $MoS_{2(1-x)}Se_{2x}$ monolayers with $x = 0.15$ and $x = 0.30$ (Figure 5d,f). The mobility of all $MoS_{2(1-x)}Se_{2x}$ monolayer FETs can be improved by further minimizing the contact resistance[33–35] and using high-κ top-gating (κ = dielectric constant).[32] Addtionally, the threshold gate voltage at higher Se composition is more negative (SI: Figure S6), indicating different valence band (VB) and conduction band (CB) positions for the $MoS_{2(1-x)}Se_{2x}$ monolayers with different Se compositions.

In conclusion, we have grown triangular domains and continuous films of 2D $MoS_{2(1-x)}Se_{2x}$ ($0 \le x \le 0.40$) semiconductor alloys. Atomic-resolution STEM revealed random arrangement of the S and Se atoms around the Mo atoms. Tunable bandgap emissions were observed. Electrical measurement confirmed semiconductive behavior for all as-grown $MoS_{2(1-x)}Se_{2x}$ monolayers. This work enables fabrication of large-area optoelectronic devices, such as light-detection device arrays and thin-film solar cells by stacking 2D materials with optimized bandgaps and VB/CB positions.[36,37]

Experimental Section

Sample Growth: $MoS_{2(1-x)}Se_{2x}$ monolayers were synthesized by evaporation of powders of $MoSe_2$ (Sigma-Aldrich, 99.95%, 40 μm) and MoS_2 (Sigma-Aldrich, 99%, <2 μm) at temperatures higher than 940 °C in the first and second heating zones, respectively (see Figure 1). The loading amount of the MoS_2 and $MoSe_2$ powders was usually 10–100 mg. The SiO_2/Si substrates (oxide thickness of ~270 nm) were put in the third zone without heating for $MoS_{2(1-x)}Se_{2x}$ growth. The SiO_2/Si substrate was annealed at 800 °C for 8 h. The growth zone was at a temperature of 600–700 °C and temperature gradient was ~50 °C/cm. The carrier gases were Ar (2 sccm) and H_2 (0.5 sccm). The pressure of the growth system was ~8 Pa. Growth time was usually 10 min.

Characterization: Optical images were taken on an Olympus BX51 microscope using a 100× objective. Tapping-mode AFM was done on a Vecoo IIIa or a DI 3100 multimode microscope. SEM imaging was done on a Hitachi S4800 with a field-emission gun. Raman and PL spectra were measured on a JY Horiba HR800 micro-Raman spectroscope (514 nm excitation) under ambient conditions at room temperature. XPS was done on an Axis Ultra system.

HAADF-STEM Imaging: The monolayers were transferred onto specially-designed TEM grids made from films of carbon nanotubes supplied by Tsinghua-Foxconn Nanotechnology Research Center. HAADF-STEM imaging was done with a probe-corrected JEOL ARM-200CF with a cold-FEG operated at 80 kV.

Electrical Measurements: Electrode patterns were generated by electron beam lithography (EBL). 5 nm Ti and 50 nm Au were thermally evaporated for contacts. Devices were put in vacuum (Janis ST500 probe station, $<10^{-5}$ Torr) and measured by an Agilent B1500A semiconductor device analyzer.

Supporting Information

Supporting Information is available from the Wiley Online Library or from the author.

Acknowledgements

J.Z. acknowledges the NSFC (Nos. 21233001 and 21129001). L.X. acknowledges the NSFC (Nos. 21373066 and 11304052), the Beijing Natural Science Foundation (No. 2132056), the 973 program (No. 2011CB932803), the "Strategic Priority Research Program" of the Chinese Academy of Sciences (No. XDA09040300) and China Postdoctoral Science Foundation (No. 2014M540900). C.J. and F.L. acknowledge the NSFC (Nos. 51222202 and 61172011), the 973 Program (No. 2014CB932500), the Program for an Innovative Research Team in a University of MOE of China (No. IRT13037), and Prof. L. Gu in Institute of Physics, CAS for his assistance on STEM imaging.

Note: The authors noticed that similar papers (Adv. Mater. doi: 10.1002/adma.201304389; Nano Lett., 2014, 14 (2), pp 442–449) were published after this manuscript had been submitted. Equation 2 was presented incorrectly in the version of this work originally published online. This has been corrected here.

Received: December 12, 2013
Revised: January 9, 2014
Published online: February 20, 2014

[1] S. Z. Butler, S. M. Hollen, L. Y. Cao, Y. Cui, J. A. Gupta, H. R. Gutierrez, T. F. Heinz, S. S. Hong, J. X. Huang, A. F. Ismach, E. Johnston-Halperin, M. Kuno, V. V. Plashnitsa, R. D. Robinson, R. S. Ruoff, S. Salahuddin, J. Shan, L. Shi, M. G. Spencer, M. Terrones, W. Windl, J. E. Goldberger, *ACS Nano* **2013**, *7*, 2898–2926.

[2] Q. H. Wang, K. Kalantar-Zadeh, A. Kis, J. N. Coleman, M. S. Strano, *Nat. Nanotechnol.* **2012**, *7*, 699–712.

[3] M. S. Xu, T. Liang, M. M. Shi, H. Z. Chen, *Chem. Rev.* **2013**, *113*, 3766–3798.

[4] K. F. Mak, K. L. He, C. Lee, G. H. Lee, J. Hone, T. F. Heinz, J. Shan, *Nat. Mater.* **2013**, *12*, 207–211.

[5] K. F. Mak, K. L. He, J. Shan, T. F. Heinz, *Nat. Nanotechnol.* **2012**, *7*, 494–498.

[6] T. Cao, G. Wang, W. P. Han, H. Q. Ye, C. R. Zhu, J. R. Shi, Q. Niu, P. H. Tan, E. Wang, B. L. Liu, J. Feng, *Nat. Commun.* **2012**, *3*, 887.

[7] H. L. Zeng, J. F. Dai, W. Yao, D. Xiao, X. D. Cui, *Nat. Nanotechnol.* **2012**, *7*, 490–493.

[8] N. N. Mao, Y. F. Chen, D. M. Liu, J. Zhang, L. M. Xie, *Small* **2013**, *9*, 1312–1315.

[9] O. Lopez-Sanchez, D. Lembke, M. Kayci, A. Radenovic, A. Kis, *Nat. Nanotechnol.* **2013**, *8*, 497–501.

[10] X. Huang, Z. Y. Zeng, H. Zhang, *Chem. Soc. Rev.* **2013**, *42*, 1934–1946.

[11] H. P. Komsa, A. V. Krasheninnikov, *J. Phys. Chem. Lett.* **2012**, *3*, 3652–3656.

[12] J. Kang, S. Tongay, J. B. Li, J. Q. Wu, *J. Appl. Phys.* **2013**, *113*, 143703–143707.

[13] Y. F. Chen, J. Y. Xi, D. O. Dumcenco, Z. Liu, K. Suenaga, D. Wang, Z. G. Shuai, Y. S. Huang, L. M. Xie, *ACS Nano* **2013**, *7*, 4610–4616.

[14] K. Yan, L. Fu, H. L. Peng, Z. F. Liu, *Acc. Chem. Res.* **2013**, *46*, 2263–2274.

[15] X. S. Li, W. W. Cai, J. H. An, S. Kim, J. Nah, D. X. Yang, R. Piner, A. Velamakanni, I. Jung, E. Tutuc, S. K. Banerjee, L. Colombo, R. S. Ruoff, *Science* **2009**, *324*, 1312–1314.

[16] S. Bae, H. Kim, Y. Lee, X. F. Xu, J. S. Park, Y. Zheng, J. Balakrishnan, T. Lei, H. R. Kim, Y. I. Song, Y. J. Kim, K. S. Kim, B. Ozyilmaz, J. H. Ahn, B. H. Hong, S. Iijima, *Nat. Nanotechnol.* **2010**, *5*, 574–578.

[17] A. Reina, X. T. Jia, J. Ho, D. Nezich, H. B. Son, V. Bulovic, M. S. Dresselhaus, J. Kong, *Nano Lett.* **2009**, *9*, 30–35.

[18] S. Najmaei, Z. Liu, W. Zhou, X. L. Zou, G. Shi, S. D. Lei, B. I. Yakobson, J. C. Idrobo, P. M. Ajayan, J. Lou, *Nat. Mater.* **2013**, *12*, 754–759.

[19] A. M. van der Zande, P. Y. Huang, D. A. Chenet, T. C. Berkelbach, Y. M. You, G. H. Lee, T. F. Heinz, D. R. Reichman, D. A. Muller, J. C. Hone, *Nat. Mater.* **2013**, *12*, 554–561.

[20] Y. M. Shi, W. Zhou, A. Y. Lu, W. J. Fang, Y. H. Lee, A. L. Hsu, S. M. Kim, K. K. Kim, H. Y. Yang, L. J. Li, J. C. Idrobo, J. Kong, *Nano Lett.* **2012**, *12*, 2784–2791.

[21] X. S. Wang, H. B. Feng, Y. M. Wu, L. Y. Jiao, *J. Am. Chem. Soc.* **2013**, *135*, 5304–5307.

[22] K. K. Liu, W. J. Zhang, Y. H. Lee, Y. C. Lin, M. T. Chang, C. Su, C. S. Chang, H. Li, Y. M. Shi, H. Zhang, C. S. Lai, L. J. Li, *Nano Lett.* **2012**, *12*, 1538–1544.

[23] S. F. Wu, C. M. Huang, G. Aivazian, J. S. Ross, D. H. Cobden, X. D. Xu, *ACS Nano* **2013**, *7*, 2768–2772.

[24] K. F. Mak, C. Lee, J. Hone, J. Shan, T. F. Heinz, *Phys. Rev. Lett.* **2010**, *105*, 136805.

[25] C. Lee, H. Yan, L. E. Brus, T. F. Heinz, J. Hone, S. Ryu, *ACS Nano* **2010**, *4*, 2695–2700.

[26] Y. Chen, D. O. Dumcenco, Y. Zhu, X. Zhang, N. Mao, Q. Feng, M. Zhang, J. Zhang, P. Tan, Y.-S. Huang, L. Xie, *Nanoscale* **2013**, DOI: 10.1039/C1033NR05630A.

[27] R. Loudon, *Adv. Phys.* **2001**, *50*, 813–864.

[28] S. Tongay, J. Zhou, C. Ataca, K. Lo, T. S. Matthews, J. B. Li, J. C. Grossman, J. Q. Wu, *Nano Lett.* **2012**, *12*, 5576–5580.

[29] D. O. Dumcenco, H. Kobayashi, Z. Liu, Y. S. Huang, K. Suenaga, *Nat. Commun.* **2013**, *4*, 1351.

[30] O. L. Krivanek, M. F. Chisholm, V. Nicolosi, T. J. Pennycook, G. J. Corbin, N. Dellby, M. F. Murfitt, C. S. Own, Z. S. Szilagyi, M. P. Oxley, S. T. Pantelides, S. J. Pennycook, *Nature* **2010**, *464*, 571–574.

[31] S. Wurmehl, J. T. Kohlhepp, H. J. M. Swagten, B. Koopmans, M. Wojcik, B. Balke, C. G. F. Blum, V. Ksenofontov, G. H. Fecher, C. Felser, *Appl. Phys. Lett.* **2007**, *91*, 052506.

[32] B. Radisavljevic, A. Radenovic, J. Brivio, V. Giacometti, A. Kis, *Nat. Nanotechnol.* **2011**, *6*, 147–150.

[33] S. Das, H. Y. Chen, A. V. Penumatcha, J. Appenzeller, *Nano Lett.* **2013**, *13*, 100–105.

[34] W. Liu, J. H. Kang, D. Sarkar, Y. Khatami, D. Jena, K. Banerjee, *Nano Lett.* **2013**, *13*, 1983–1990.

[35] Y. Yoon, K. Ganapathi, S. Salahuddin, *Nano Lett.* **2011**, *11*, 3768–3773.

[36] M. Bernardi, M. Palummo, J. C. Grossman, *Nano Lett.* **2013**, *13*, 3664–3670.

[37] L. Britnell, R. M. Ribeiro, A. Eckmann, R. Jalil, B. D. Belle, A. Mishchenko, Y. J. Kim, R. V. Gorbachev, T. Georgiou, S. V. Morozov, A. N. Grigorenko, A. K. Geim, C. Casiraghi, A. H. C. Neto, K. S. Novoselov, *Science* **2013**, *340*, 1311–1314.